Pseudo-global tomography for local micro-computed tomography with high-brightness synchrotron X-rays

Wenhao Chen (陈文豪)[1,2], Yudan Wang (王玉丹)[1], Huiqiang Liu (刘慧强)[1], Biao Deng (邓 彪)[1], Yushuang Yang (杨玉双)[3], and Tiqiao Xiao (肖体乔)[1,2,*]

[1] *Shanghai Synchrotron Radiation Facility, Shanghai Institute of Applied Physics, Chinese Academy of Sciences, Shanghai 201204, China*

[2] *University of Chinese Academy of Sciences, Beijing 100049, China*

[3] *CSIRO Materials Science and Engineering, Private Bag 33, Clayton South, Victoria 3169, Australia*

[*] *Corresponding author: tqxiao@sinap.ac.cn*

Received July 26, 2013; accepted December 12, 2013; posted online January 23, 2014

The computed tomography imaging of a local region inside a sample with a size larger than the field of view is particularly important for synchrotron X-ray imaging. In this letter, an improved algorithm is proposed to reconstruct the local structure inside a sample using almost completely local data. The algorithm significantly reduces the X-ray radiation dose and improves computational efficiency. Simulation results show that the new algorithm works well and has a higher reconstruction precision than previous methods, as confirmed by experimental results carried out at the Shanghai Synchrotron Radiation Facility.

OCIS codes: 340.7440, 110.6960, 100.3010, 340.6720.

doi: 10.3788/COL201412.023401.

Synchrotron radiation (SR) computed tomography (CT) is an effective, sample, non-destructive, cross-sectional imaging tool with wide-ranging applications in medicine, biology, and industry[1,2]. Nevertheless, the detector has a limited field of view (FOV) because of current hardware limitations[3]. The CT imaging of a local region inside a sample with size larger than the the FOV is particularly important for synchrotron X-ray imaging to achieve high resolution while maintaining sample integrity. However, the conventional filtered back projection (FBP) algorithm is inadequate for correctly reconstructing local CT projections because of its nonlocal property[3].

Several approaches have been proposed to solve the local CT reconstruction problem. However, some of these algorithms only work well at the jumping points of the original density function[4,5]; some require extra knowledge[6−8] that make them difficult to implement; others require projections to be extrapolated[9,10]. To date, an optimized extrapolation method for high-precision reconstruction is lacking.

In this letter, an improved algorithm aimed at overcoming the abovementioned shortcomings of available methods is proposed. The algorithm uses an effective strategy to compensate for the lost part of projections in a local CT, which can effectively reduce DC shift and low-frequency artifacts caused by projection truncation. The new algorithm reconstructs the correct inner structure of the sample throughout the entire region of interest (ROI) without prior knowledge of it. Moreover, only the ROI instead of the entire sample is reconstructed, which improves computational efficiency.

Using the Fourier slice theorem[11], $f(x)$ can be recovered from values of its Radon transform through Radon's celebrated classical formula

$$f(x) = -\frac{1}{\pi}\lim_{\varepsilon\to 0}\int_{\varepsilon}^{\infty}\frac{\mathrm{d}F_x(t)}{t}, \quad t\in R, x\in R^2, \tag{1}$$

where $F_x(t)$ is the average of all integrals of f over lines apart from point x with distance t, leading to the relation[12]

$$-\frac{1}{\pi}\int_{\varepsilon}^{\infty}\frac{\mathrm{d}F_x(t)}{t} = \Phi_\varepsilon * f(x), \tag{2}$$

where * means convolution, Φ_ε is a positive radial kernel, $\Phi_\varepsilon(x) = \varepsilon^{-2}\Phi(x/\varepsilon)$, $\Phi(x) = \chi(|x|)/(\pi^2|x|^2\sqrt{|x|^2-1})$, and $\chi(t)=\begin{cases}0 & if\ |t|\leqslant 1\\ 1 & if\ |t|>1.\end{cases}$ Equation (2) can be used as the basis for localized reconstruction from Radon transformed data. Defining $\Psi(x) = 4\Phi(2x) - \Phi(x), \quad x\in R^2$, then according to Eq. (2),

$$\Psi * f(a,x) = \Psi_a * f(x) = -\frac{1}{\pi}\int_{a/2}^{a}\frac{\mathrm{d}F_x(t)}{t}. \tag{3}$$

For any positive ε, we have

$$\sum_{j=-\infty}^{\infty}\Psi * f(2^j\varepsilon, x) = f(x). \tag{4}$$

As long as j is sufficiently large, $\Psi * f(2^j\varepsilon, x)$ contains mainly low-frequency information[12] that could be ignored remaining sufficiently high reconstruction precision. Thus, we can use the projections on lines passing through the region of exposure (ROE, which is ROI plus an extra margin) to reconstruct the ROI.

Focus is then given to the width of the extra margin. Through the convolution theorem, Eq. (1) can be rewritten as

$$f(x) = \int_0^{\pi}\int_{-\infty}^{\infty} Rf(\theta,t)\times h(\langle x,u_\theta\rangle - t)\mathrm{d}t\mathrm{d}\theta, \tag{5}$$

where $u_\theta = (\cos\theta, \sin\theta)$, $\langle x, u_\theta\rangle$ is the usual scalar product of x and u_θ, $Rf(\theta,t)$ is the integral of f over lines

that are t apart from the original point at angle θ, and h is the convolution kernel. In practice, the convolution kernel h can be expressed as[11]

$$h(md) = \begin{cases} 1/(4d^2) & m = 0 \\ 0 & m = even \\ -1/(\pi dm)^2 & m = odd \end{cases}, \quad (6)$$

where m is an integer, and d is the sampling interval of the projected images that equals the pixel size. In local CT reconstruction, the poorest deviation occurs at the margin of the ROI nearest to the lost parts of the projections. From the convolution given by Eq. (5), this deviation could be attributed to $h(md)$, which has a part outside the FOV. To evaluate the influence of this part of h, denoting the part of $h(md)$ outside the FOV as $m \in (-\infty, -n) \cup (N, +\infty)$, the energy leakage of h is defined as

$$s(n) = \sum_{m=-\infty}^{m=-n} |h(md)| / \sum_{m=-\infty}^{m=\infty} |h(md)| + \sum_{m=N}^{m=\infty} |h(md)| / \sum_{m=-\infty}^{m=\infty} |h(md)|, \quad (7)$$

where N is a large number, and the second term on the right side of Eq. (7) is very small and can be ignored. In this letter, if $s \leqslant 0.01$, we believe that the influence of the part of h outside the FOV can be ignored. According to Eq. (7), the energy leakage is less than 0.01 when $n \geqslant 9$, indicating that the width of the ROI's extra margin should be no less than 9 pixels. Accordingly, the ROE in this letter is defined as ROI plus an extra margin of 10 pixels. Compared with conventional CT requiring the entire sample in the ROE, the X-ray radiation dose is significantly reduced.

CT reconstruction from a truncated sinogram is known to generally lead to artifacts in slice in the form of a global (i.e., feature independent) elevation of the gray values toward the edge of the reconstructed ROI[13]. This kind of artifacts is due to the loss of low-frequency information that can be suppressed by projection extension[14].

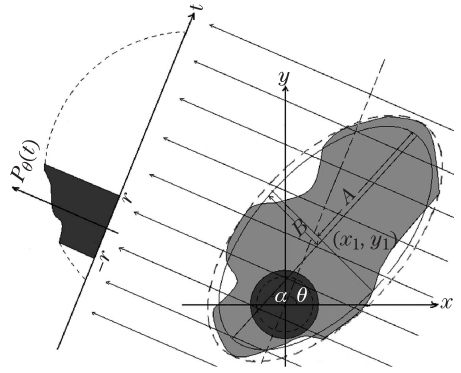

Fig. 1. Example of a projection $P_\theta(t)$. The solid and dashed lines show the truncated projection and extended part, respectively. The solid ellipse shows the simulated configuration of the sample including the ROE (solid circle, which is the ROI (dashed circle) plus 10 more extra pixels), which generally does not exceed the wrap of the sample (dashed ellipse). The gray irregular area shows the actual sample shape.

In this letter, an elliptic projection extension method is proposed, as shown in Fig. 1. The ellipse is generally very close to the actual shape of samples. Thus, the difference between the ellipse and real sample shape can be controlled to the least value, which usually occurs around the margin and normally far from ROI. According to the previous analysis, the effect of lost projections could be ignored when it is far from the ROI. The choice of the elliptic long half-shaft and short half-shaft depends on the length and width of the sample. The extended parts of the projections should be continuous at the ends of the truncated projections, and the value of the extension is proportional to the path length of X-ray inside the ellipse. According to the geometry mathematics in Fig. 1, the projection extension is given as

$$P''_\theta(t) = \begin{cases} \dfrac{P'_{\theta-\alpha}(t - s\cos(\gamma-\theta))}{P'_{\theta-\alpha}(r - s\cos(\gamma-\theta))} P_\theta(r) & t > r \\ P_\theta(t) & |t| \leqslant r \\ \dfrac{P'_{\theta-\alpha}(t - s\cos(\gamma-\theta))}{P'_{\theta-\alpha}(-r - s\cos(\gamma-\theta))} P_\theta(-r) & t < -r \end{cases}, \quad (8)$$

where r is the radius of the FOV, $P_\theta(t)$ is the truncated projection we obtain, $P'_\theta(t)$ is the path length of X-ray that is perpendicular to distance t away from the original point at projection angle θ, which can be expressed as

$$P'_\theta(t) = \begin{cases} \dfrac{2AB\sqrt{A^2\cos^2\theta + B^2\sin^2\theta - t^2}}{A^2\cos^2\theta + B^2\sin^2\theta} \\ |t| \leqslant \sqrt{A^2\cos^2\theta + B^2\sin^2\theta} \\ 0 \\ |t| > \sqrt{A^2\cos^2\theta + B^2\sin^2\theta} \end{cases}, \quad (9)$$

where $s = \sqrt{x_1^2 + y_1^2}$, $\gamma = \tan^{-1}(y_1/x_1)$, (x_1, y_1) is the center of the ellipse and the original point is the center of the FOV, and α is the angle between the long shaft of the ellipse and the X-axis.

For the special case, i.e., where the density distribution inside the sample is annular, the density at different annuli differ from one another and result in a sudden increase or decrease among the different parts of a projection. Accordingly, Eq. (9) can be rewritten as

$$P''_\theta(t) = \begin{cases} \sum\limits_{k=1}^{n} \dfrac{cP'_{\theta-\alpha}(t - s\cos(\gamma-\theta))}{nP'_{\theta-\alpha}(r - (k-1)d - s\cos(\gamma-\theta))} \\ P_\theta(r - (k-1)d) \quad t > r \\ P_\theta(t) \quad |t| \leqslant r \\ \sum\limits_{k=1}^{n} \dfrac{cP'_{\theta-\alpha}(t - s\cos(\gamma-\theta))}{nP'_{\theta-\alpha}(-r + (k-1)d - s\cos(\gamma-\theta))} \\ P_\theta(-r + (k-1)d) \quad t < -r \end{cases}, \quad (10)$$

where c is a constant and $c > 0$, $n \geqslant 1$, d is the sampling step in the projected image, and $0 \leqslant (n–1)d < r$.

The Shepp-Logan head phantom (256×256) is adopted as the test phantom. Two different ROIs are selected for the simulation, as shown in Fig. 2(a). A total of 360 local projections are generated during the simulation with an angle sampling step of 0.5°.

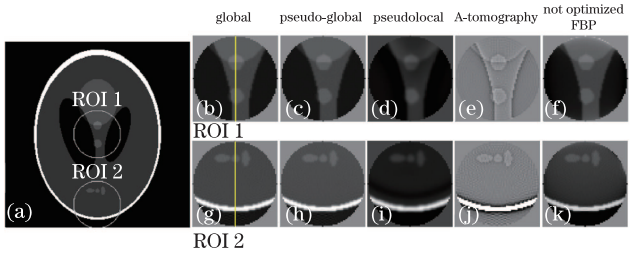

Fig. 2. Phantom and reconstructed ROIs (65 × 65 pixels). (a) Phantom, with the white circles indicating the ROIs; (b, g) images reconstructed by global CT with global projections; (c, h) pseudo-global tomography; (d, i) pseudolocal tomography; (e, j) Λ-tomography; (f, k) notoptimized FBP.

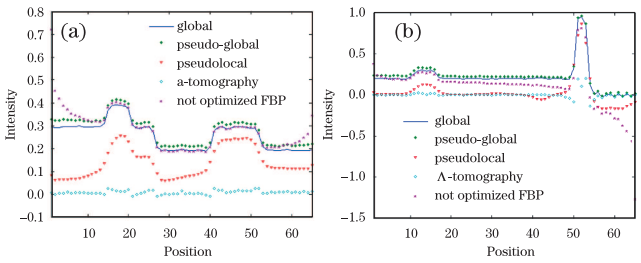

Fig. 3. Intensity profiles along the vertical central lines through the ROIs shown in Fig. 2, where the profiles for ROI 1 (a) and ROI 2 (b) are given.

Figure 2 shows the ROIs reconstructed by different local algorithms. For comparison, ROIs from global reconstruction are also given. The ROIs reconstructed by pseudo-global tomography are obviously very close to that reconstructed by global CT, whereas the images from pseudolocal tomography and Λ-tomography do not work well in smooth areas. The images from the notoptimized FBP tomography[9] (using FBP method to perform local reconstruction requiring projection extension; "notoptimized FBP" means this local method's projection extension is not optimized) have an apparent image distortion at the margin. To more clearly visualize the details, the central vertical intensity profiles of the ROIs shown in Fig. 2 are displayed in Fig. 3. All profiles of pseudo-global tomography at all areas are reconstructed with relatively high precision, but a constant deviation occurs. For the other local algorithms, a clear distortion is observed.

To quantitatively evaluate the similarity between the global and local CTs, the normalized cross correlation (NCC)[15] is used. NCC is commonly used for image analysis. The NCC between two different images (f and t) of size $m \times n$ is defined by

$$\gamma(f,t)=\frac{\sum_{i=1}^{m}\sum_{j=1}^{n}(f(i,j)-\mu_f)\cdot(t(i,j)-\mu_t)}{\{[\sum_{i=1}^{m}\sum_{j=1}^{n}(f(i,j)-\mu_f)^2]\cdot[\sum_{i=1}^{m}\sum_{j=1}^{n}(t(i,j)-\mu_t)^2]\}^{1/2}}, \tag{11}$$

where $\mu_f=\sum_{i=1}^{m}\sum_{j=1}^{n}f(i,j)/(m\cdot n)$ and $\mu_t=\sum_{i=1}^{m}\sum_{j=1}^{n}t(i,j)/(m\cdot n)$. The NCC is confined between −1 and +1. A larger NCC indicates a higher similarity between the two images. Taking the ROIs from the global CT as the references, the NCCs for the ROIs from the local CT algorithms are given in Table 1.

Table 1 shows that the highest reconstruction precision could be achieved using the proposed algorithm, in accordance with the abovementioned analysis. Table 1 also shows that pseudo-global tomography works well for different sample areas, whereas the precision differs from one another for different ROIs in the other methods.

The experiments were carried out at the X-ray imaging beamline BL13W at the Shanghai Synchrotron Radiation Facility, as shown in Fig. 4(a). Figure 4(b) is the schematic of the local tomography. The effective pixel size of detector is 3.7 × 3.7 μm^2. A phantom is specially designed for the experiments, in which the outermost layer is a polyamide-Nylon6 (PA6) tube with diameter $\phi_{\rm out}$ = 2.77 mm, $\phi_{\rm in}$ = 1.87 mm, the interlining is a polytetrafluoroethylene tube with $\phi_{\rm out}$ = 1.82 mm, ϕ_{in} = 1.0 mm, and the middle part is 14 pieces of PET filaments with ϕ = 0.1 mm.

In the experiments, the X-ray photon energy was set to 14.5 keV, and 720 projections of the entire sample over a total rotation angle of 180° were collected at 0.25° angular step. A reconstructed slice of the sample is shown in Fig. 5(a). Similar to that in simulation, two characteristic regions were chosen as ROIs. The local projections of the ROIs were obtained by truncating the full projections of the entire sample. Figure 5 presents the ROIs reconstructed from different local CT algorithms. The simulation results given in the previous section could be confirmed by experiments. The ROIs from the pseudo-

Table 1. NCCs of ROIs for Different Algorithms

ROI	Pseudo-global	Pseudolocal	Λ-tomography	Notoptimized FBP
ROI 1	0.9992	0.9423	0.6239	0.9421
ROI 2	0.9992	0.9693	0.8199	0.8518

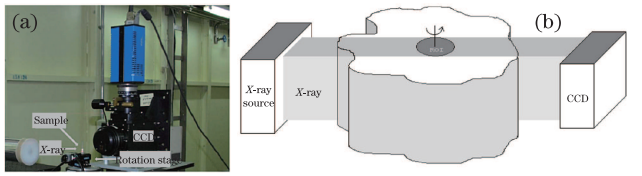

Fig. 4. Experimental facilities at the Shanghai Synchrotron Radiation Facility BL13W beamline and schematic of the local tomography.

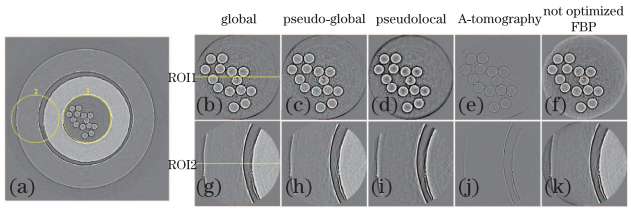

Fig. 5. Experimental results for the phantom, where (a) is the global CT slice for the entire sample in which the two ROIs are indicated; (b) and (g) show the ROIs taken from global reconstruction with 258 × 258 pixels; the other slices are taken from pseudo-global tomography (c, h), pseudolocal tomography (d, i), Λ-tomography (e, j), and notoptimized FBP (f, k).

global tomography are the closest reconstruction to the global tomography. The ROIs from pseudolocal tomography and Λ-tomography lose most of the information in smooth areas. Image distortion is easily observed in ROIs from the unoptimized FBP in the margin.

The reconstructed intensity profiles from local tomography are given in Figs. 6(a) and 6(c), in which the correspondent profiles from global CT are also given for reference. To compare the precision of all local CT methods, intensity deviations from the global CT are also presented in Figs. 6(b) and (d). Obviously, pseudo-global tomography could work well and achieve good reconstruction precision at all regions inside the ROIs. A constant bias to the global CT occurs for the pseudo-global tomography, which is inevitable in the local reconstruction using inverse Radon transformation[16]. Using a known material to calibrate the reconstruction, this local CT method can still be used for quantitative X-ray imaging. Similar to that in simulation, NCC is also given to evaluate the accuracy of the reconstructions, as shown in Table 2. The experimental results in Table 2 confirm the above analysis based on simulation, which shows that pseudo-global CT has better precision at different kinds of ROI.

In conclusion, an improved algorithm called pseudo-global tomography is developed to reconstruct the ROI in a sample with essentially local data. Numerical simulation and experiments are carried out to evaluate the validity and efficiency of the proposed algorithm. Results show that the new local CT method works well and has high reconstruction precision regardless of the location of the ROI in the sample. The non-uniqueness of the interior problem leads to the inevitable existence of a constant bias in the reconstructed ROI image. However, this bias could be corrected through a calibration process by introducing a known material. In this way, the proposed pseudo-global tomography could still be used for quantitative CT imaging. Combining with other advantages, the proposed pseudo-global algorithm for local tomography could find its extensive applications in biomedical and material sciences.

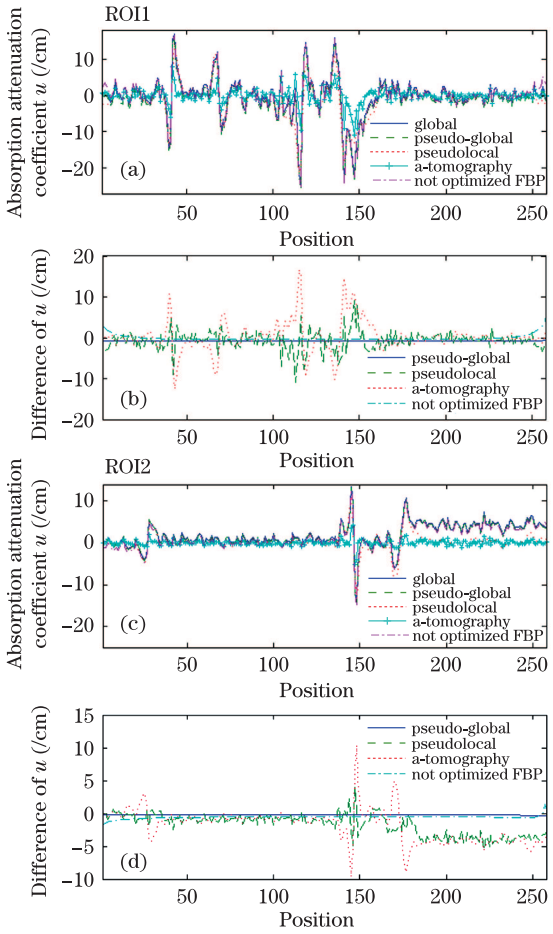

Fig. 6. (a, c) Intensity profiles along the horizontal central lines through the ROIs, as shown in Fig. 5 and (b, d) the deviations of intensities from the local tomography to that from global tomography.

Table 2. NCC of ROIs for Different Algorithms in the Experiments

ROI	Pseudo-global	Pseudolocal	Λ-tomography	Unoptimized FBP
ROI 1	0.9999	0.9129	0.8411	0.9543
ROI 2	0.9999	0.8896	0.7681	0.9895

This work was supported by the National Basic Research Program of China (No. 2010CB834301), the National Natural Science Foundation of China (No. U1232205 and 11105213), and the CAS-CSIRO cooperation research project (No. GJHZ1303).

References

1. H. Liu, Y. Ren, H. Guo, Y. Xue, H. Xie, T. Xiao, and X. Wu, Chin. Opt. Lett. **10,** 121101 (2012).
2. R. C. Chen, L. Kigon, and R. Longo, Opt. Express **21,** 7384 (2113).
3. L. Q. Li, H. Toda, T. Ohgaki, M. Kobayashi, and T. Kobayashi, J. Appl. Phys. **102,** 114908 (2007).
4. A. Faridani, E. L. Ritman, and K. T. Smith, SIAM J. Appl. Math. **52,** 459 (1992).
5. A. I. Katsevich and A. G. Ramm, SIAM J. Appl. Math. **56**, 167 (1996).
6. A. H. Delaney and Y. Bresler, IEEE Trans. Image Processing **4,** 799 (1995).
7. E. A. Rashed and H. Kudo, J. Synchrotron Radiat. **20,** 116 (2013).
8. M. Defrise, F. Noo, R. Clackdoyle, and H. Kudo, Inverse Probl. **22,** 1037 (2006).
9. A. Kyrieleis, V. Titarenko, M. Ibison, T. Connolley, and P. J. Withers, J. Microsc. **241,** 69 (2011).
10. Z. Chen, Opt. Eng. **47,** 017001 (2008).
11. A. C. Kak and M. Slaney, *Principles of Computerized Tomographic Imaging* (IEEE Press, New York, 1988).
12. W. R. Madych, Appl. Comput. Harmon. A **7,** 54 (1999).
13. R. M. Lewitt and R. H. T. Bates, Optik, Stuttgart **50,** 189 (1978).
14. R. M. Lewitt, Med. Phys. **6,** 412 (1979).
15. J. C. Yoo and T. H. Han, Circ. Syst. Signal Pr. **28,** 819 (2009).
16. F. Natterer, *The Mathematics of Computerized Tomography* (Wiley, New York, 1986).